

Confronting General Relativity with Further Cosmological Data

Scott F. Daniel¹ and Eric V. Linder^{1,2,3}

¹*Institute for the Early Universe, Ewha Womans University, Seoul, Korea*

²*Lawrence Berkeley National Laboratory, Berkeley, CA, USA*

³*Berkeley Center for Cosmological Physics, University of California, Berkeley, CA, USA*

(Dated: February 5, 2022)

Deviations from general relativity in order to explain cosmic acceleration generically have both time and scale dependent signatures in cosmological data. We extend our previous work by investigating model independent gravitational deviations in bins of redshift and length scale, by incorporating further cosmological probes such as temperature-galaxy and galaxy-galaxy cross-correlations, and by examining correlations between deviations. Markov Chain Monte Carlo likelihood analysis of the model independent parameters fitting current data indicates that at low redshift general relativity deviates from the best fit at the 99% confidence level. We trace this to two different properties of the CFHTLS weak lensing data set and demonstrate that COSMOS weak lensing data does not show such deviation. Upcoming galaxy survey data will greatly improve the ability to test time and scale dependent extensions to gravity and we calculate the constraints that the BigBOSS galaxy redshift survey could enable.

I. INTRODUCTION

Gravitation is the key force governing the expansion and evolution of the universe. The unexpected observations of cosmic acceleration may indicate that some aspects of this fundamental force remain a mystery. General relativity is a hugely successful theory of gravity over the ranges it has been tested, but we should continue to test it in greater detail in regions, such as on cosmic scales, where it has not been sufficiently probed.

Since it is not clear what form deviations from general relativity (GR) may take, it is useful not only to adopt specific models extending GR but also to consider model independent approaches. These generally parameterize the relation between the metric potentials, the relation between the potentials and the matter density, or similar forms. A translation table between many of the most common conventions was provided in [1].

The effects giving rise to cosmic acceleration must take place on the largest length scales, but general relativity is known to be highly accurate on small scales (solar system and laboratory), so the deviations must have scale dependence. This can either be innate (from the scale dependence in the Poisson equation), or explicit. Similarly, conditions in the early universe such as during primordial nucleosynthesis or recombination can be well explained within GR, and acceleration is a recent phenomenon, so the deviation from GR should also be time dependent.

In this article we broaden consideration of the deviation parametrization, and convert to more observationally direct variables than used in [1]. In Sec. II we examine some possible time and space dependencies and examine the correlation between the deviation variables. By adopting a model independent, binned formalism we avoid putting in ad hoc assumptions about the form of the deviation, letting the data determine the results. We consider different data types probing the matter density distribution in Sec. III, going beyond the cosmic microwave background (CMB) perturbations, Type Ia

supernova distance-redshift relation, and weak gravitational lensing used in [1]. Prospects for further improvements in constraints from future data are investigated in Sec. IV.

II. CONSTRAINING DEVIATIONS OF GRAVITY

The relations between the two metric potentials (often called the gravitational slip), the matter density and velocity fields (continuity equation), the matter density and a metric potential (Poisson equation), and velocity field and the other metric potential (Euler equation) form a system of equations describing the spacetime and its contents. Modifications to gravity adjust these interrelations and so one can parameterize these theories by inserting time and space dependent functions in the usual GR relations.

One example is to define the gravitational slip as

$$\psi = [1 + \varpi(a, k)] \phi, \quad (1)$$

where the metric is given in conformal Newtonian gauge through

$$ds^2 = a^2[-(1 + 2\psi) d\tau^2 + (1 - 2\phi) d\vec{x}^2], \quad (2)$$

and a is the scale factor, k the wavenumber, τ the conformal time, and x the spatial coordinate. Preserving stress energy conservation, and so the continuity and Euler equations, we are left with needing the Poisson equation, modified to

$$-k^2\phi = 4\pi G_N a^2 \bar{\rho}_m \Delta_m \times \mu(a, k), \quad (3)$$

where G_N is Newton's constant, $\bar{\rho}_m$ is the homogeneous part of the matter density and Δ_m the perturbed part written in gauge-invariant form, i.e.

$$\Delta_m \equiv \delta_m + \frac{3\mathcal{H}\theta_m}{k^2} \quad (4)$$

in the notation of [2], where θ_m is the velocity perturbation and \mathcal{H} is the conformal Hubble parameter.

These two functions, ϖ and μ , were used in [1] and several other papers, and are equivalent to many other parametrizations as detailed in the translation table of [1]. In this paper, we will present a few further results using these variables, but the bulk of the paper will use “decorrelated” parameters based on these.

A. ϖ and μ as Variables

One of the main focuses in [1] was to test consistency with GR. For this, only one of ϖ or μ were varied at a time. Since a shift in ϖ could be compensated by a corresponding shift in μ (see Fig. 2 of [1], or the degeneracy line in their Fig. 7) to preserve the observational agreement, the intent of varying one at a time was to make it more difficult to achieve agreement with GR and hence provide a more conservative result. Despite this “handicapping”, agreement with GR indeed occurred.

In Fig. 1 we show what happens when μ is allowed to vary simultaneously with ϖ , treating both functions as being composed of constant values within each of three redshift bins ($z < 1$, $1 < z < 2$, and $2 < z < 9$, with $z > 9$ fixed to GR). To compare to [1], we use data constraints from WMAP 5 year CMB [3–5], Union2 supernova distances [6], and COSMOS weak lensing [7] data sets. The narrow 1D distribution of ϖ recreates the fixed μ case of the middle panel of Fig. 5 of [1], while the wider distribution shows the results for ϖ when also fitting μ . The 68% cl range increases by approximately a factor of 6. The other redshift bins behave similarly. Thus, the accuracy of measurement of the deviations ϖ (and μ) is not particularly tight.

The degeneracy between the two post-GR functions is clearly seen in the 2D probability distributions of Fig. 2. The banana shape discussed in [1] persists here, even though we use independent bins of redshift rather than the a^3 functional dependence assumed in their Fig. 7. The solid black curve shows a theoretically motivated compensation relation largely responsible for the degeneracy.

We will be able to improve the constraints, and our understanding of the observational leverage on modified gravity, by “trading” precision on one combination of ϖ and μ for that of another combination. This basically corresponds to choosing variables along and perpendicular to the main degeneracy direction, as we now discuss.

B. Separating Parameter Effects: \mathcal{G} and \mathcal{V}

Several types of observables are predominantly sensitive to the sum of the potentials, e.g. the integrated Sachs-Wolfe (ISW) effect and gravitational lensing. Writing the Poisson equation in terms of such a sum yields

$$-k^2(\phi + \psi) = 8\pi G_N a^2 \bar{\rho}_m \Delta_m \times \mathcal{G}, \quad (5)$$

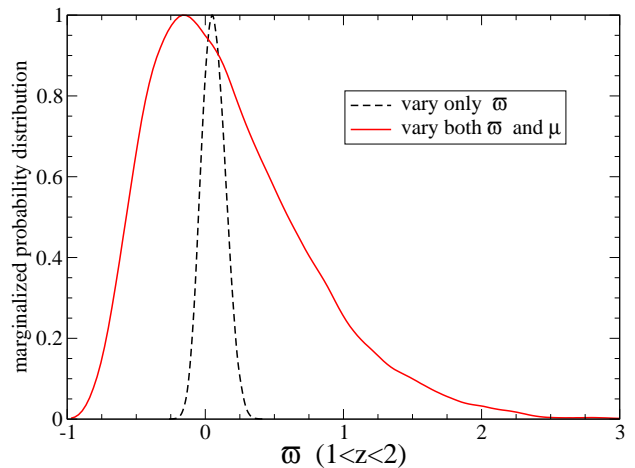


FIG. 1: 1D marginalized probability of the post-GR parameter ϖ in the redshift bin $1 < z < 2$. The narrower, dashed (black) distribution fixes the other post-GR parameter $\mu = 1$, making it more difficult to fit the data (consistent with GR) by compensating one parameter with another. The wider, solid (red) distribution includes a simultaneous fit for μ . All other cosmological parameters, including ϖ and μ in the lower and higher redshift bins, are marginalized over.

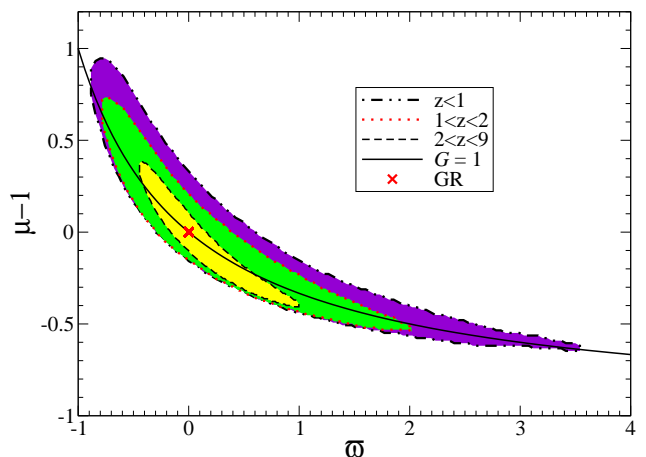


FIG. 2: 2D joint probability contours at 95% cl between the post-GR functions ϖ and μ , for three independent redshift bins. Values within the redshift bins are consistent with each other and with GR (denoted by the cross at (0,0)). The solid, black curve, motivated by a modified Poisson equation, closely follows the degeneracy direction, and suggests a more insightful parametrization using variables along and perpendicular to the curve.

where Eqs. (1) and (3) show that $\mathcal{G} = \mu(2 + \varpi)/2$. It is not surprising therefore that the confidence contours in the μ - ϖ plane are banana shaped with strong curvature.

The main degeneracy curve illustrated in Fig. 2 is precisely the combination entering \mathcal{G} . Therefore it makes sense to switch variables to use this combination as one

parameter. We can also use Eqs. (5) and (3) to define a Poisson-like equation for ψ ; here we write all three equations together to show the parallelism:

$$-k^2(\phi + \psi) = 8\pi G_N a^2 \bar{\rho}_m \Delta_m \times \mathcal{G} \quad (6)$$

$$-k^2\phi = 4\pi G_N a^2 \bar{\rho}_m \Delta_m \times \mu \quad (7)$$

$$-k^2\psi = 4\pi G_N a^2 \bar{\rho}_m \Delta_m \times \mathcal{V}. \quad (8)$$

The parameter \mathcal{V} is precisely the parameter identified as mostly sensitive to growth of structure in [1] (there called Σ ; note that [8] earlier noted this set to be of interest, calling \mathcal{V} as μ , and \mathcal{G} as Σ ; [9] also explored this later). It is also closely related to the growth index parameter γ [10, 11].

The new post-GR functions are related to the old ones via

$$\mathcal{G} = \mu \frac{2 + \varpi}{2} \quad ; \quad \mu = 2\mathcal{G} - \mathcal{V} \quad (9)$$

$$\mathcal{V} = \mu(1 + \varpi) \quad ; \quad \varpi = \frac{2\mathcal{V} - 2\mathcal{G}}{2\mathcal{G} - \mathcal{V}}. \quad (10)$$

We will see that the new functions are substantially decorrelated from each other, producing more independent constraints when using the observational data. (The symbol \mathcal{G} is meant to evoke an effective Newton's constant in the total Poisson equation; \mathcal{V} recalls the ‘‘velocity’’ equation arising from the relation between the potential ψ and the matter velocity field, central to growth of structure.)

One expects that the integrated Sachs-Wolfe effect and, in large part, weak gravitational lensing data will mostly constrain \mathcal{G} (i.e. across the degeneracy direction seen in Fig. 2) and have little leverage on \mathcal{V} (i.e. along the degeneracy direction seen in Fig. 2). Probes that involve growth, such as weak gravitational lensing and the cross-correlation between the CMB and the galaxy density field, to some extent, and the galaxy-galaxy density power spectrum, should place some constraint on \mathcal{V} . From Fig. 2 one expects that current weak lensing data will not be that strong, however, so we will also investigate the role of current density field data in Sec. III. Future galaxy survey data should tighten the constraints further; see Sec. IV for further discussion.

C. Redshift and Scale Dependence

The post-GR functions will generally be functions of both time (redshift) and length scale (wavenumber). We do not necessarily want to assume a particular functional form, so we begin by allowing the values of \mathcal{G} and \mathcal{V} to take arbitrary values within independent bins of redshift z and wavemode k (also see early work by [12]).

If we examine the redshift dependence of \mathcal{G} , using no scale dependence initially, we find that the values of \mathcal{G} in different bins are positively correlated. We consider two independent redshift bins, with $0 < z < 1$ and $1 < z < 2$. For $z > 2$ we assume the GR values. The characteristics

discussed below do not change if we add a third bin at $2 < z < 9$, but the remainder of this paper uses two bins. The degeneracy direction between $\mathcal{G}(0 < z < 1)$ and $\mathcal{G}(1 < z < 2)$ corresponds roughly to a dependence on scale factor $\mathcal{G}(a) \sim a^1$, at least for $z < 2$. The function \mathcal{V} shows a negative correlation between $\mathcal{V}(0 < z < 1)$ and $\mathcal{V}(1 < z < 2)$, such that they roughly compensate each other: $\mathcal{V}(0 < z < 1) - 1 \approx -[\mathcal{V}(1 < z < 2) - 1]$.

Regarding degeneracies with other cosmological parameters, there is little correlation except with the mass fluctuation amplitude σ_8 . This accords with the principal influence of \mathcal{V} and \mathcal{G} being on growth of scalar perturbations, especially at late times. The main effect is a positive correlation between $\mathcal{V}(1 < z < 2)$ and σ_8 ; recall that \mathcal{V} is the post-GR parameter most strongly entering into the growth of Δ_m . That the higher z bin of \mathcal{V} is most correlated follows from growth being cumulative, so the higher redshift bin has a longer lever arm of influence to imprint the effects of gravitational modifications. We also find a slight negative correlation between \mathcal{G} and σ_8 . This is related to the weak lensing data, which involves the sum of the potentials as well as the growth (see the discussion at the end of Section III). For higher \mathcal{G} , lower values of σ_8 will produce comparable lensing potentials. Thus, larger \mathcal{G} does not cause σ_8 to decrease per se (the way larger \mathcal{V} amplifies growth), rather it brings lower values of σ_8 into better agreement with the data.

Now considering scale dependence, we introduce two bins in wavenumber k , running from $k = 10^{-4} - 10^{-2} \text{ Mpc}^{-1}$ and $k > 10^{-2} \text{ Mpc}^{-1}$. The low k range represents the large scales from roughly Hubble scale to matter-radiation equality horizon scale, and the high k range corresponds to scales roughly over which non-CMB probes have leverage. For example we expect that the matter power spectrum (including weak lensing) would mostly constrain the second bin. Thus in total we fit for 8 post-GR parameters: \mathcal{G} and \mathcal{V} values, each in 2 bins of z and 2 bins of k .

In Fig. 3 we plot the 68% and 95% confidence limit contours in $\{\mathcal{V}, \mathcal{G}\}$ space for all bins of z and k . These contours have been calculated generalizing the modified COSMOMC code used in [1] and incorporate WMAP7 [13], supernova Union2 [6], and CFHTLS weak lensing [14] data. The original COSMOMC was presented in [15–17] and the weak lensing data module is from [18].

From Figs. 3(a)-3(c) we see that our initial supposition that \mathcal{V} and \mathcal{G} are mostly independent (or, at least, less correlated than ϖ and μ are in Fig. 2) is correct. We also see that the constraint on \mathcal{G} is in all cases stronger than the constraint on \mathcal{V} .

The dot-dashed line on the right side of the figures corresponds to values of \mathcal{V} and \mathcal{G} for which $\mu = 0$ (see Eq. 3). This would imply that the metric is independent of matter perturbations, which seems unphysical. For the most part, restriction to $\mu > 0$ does not strongly affect the contours. However, the data considered so far is not so strong as to exclude the $\mu < 0$ region (to the right of the line) without imposing a prior. We feel the prior is

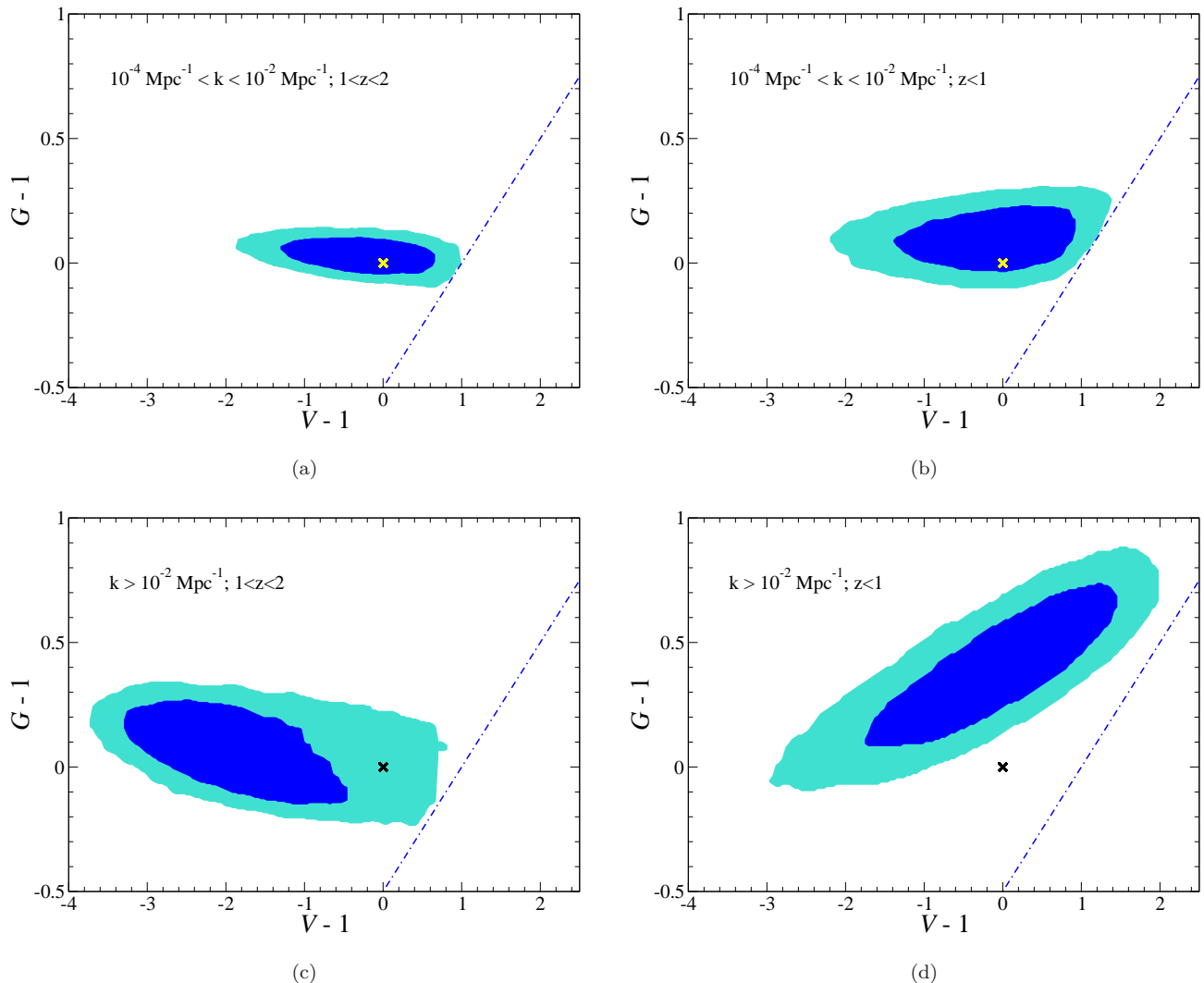


FIG. 3: 68% and 95% confidence limit contours for $\mathcal{V} - 1$ and $\mathcal{G} - 1$ are given for 2×2 binning in redshift and k space, using WMAP7 [13], Union2 [6], and CFHTLS [14] data. The diagonal, dot-dashed line denotes values of \mathcal{V} and \mathcal{G} for which $\mu = 0$ and gravity vanishes (see Eq. 3). The x's denote GR values.

justified in that, referring back to Eq. (A5) of [1], $\mu < 0$ implies (as a consequence of stress-energy conservation) that there will be some value of k for which a factor on the left hand side of that equation goes to zero, causing $\dot{\Delta}_m$ to diverge.

The upper two figures show the results for the low k bin, where the current data is most constraining. Note that GR is comfortably within the 68% cl contour. The constraints above $z \approx 1$ are slightly tighter, since the ISW effect is more sensitive to this region. The bottom two figures give the results for the high k bin, and here \mathcal{G} is significantly more constrained at higher z , again due to the ISW. Comparison of the different k bins in the same redshift range show that low k is better constrained, due to the ISW.

Figure 3(d), the high k - low z case, exhibits a number of peculiarities. It is much less constrained than the

other cases, and shows a higher correlation between \mathcal{G} and \mathcal{V} . There is also an apparent, nearly 3σ exclusion of General Relativity. Although this is a tantalizing result, it should not be taken too seriously. Since the ISW effect is an integral over redshift, the low redshift bins have very weak effects on the CMB anisotropy spectra and cannot be tightly constrained by WMAP7. Therefore, any systematic errors that create tension between the CFHTLS data and WMAP will be able to manifest themselves as non-GR values of \mathcal{V} and \mathcal{G} in these bins. Furthermore, the high k bins encompass scales for which the ISW effect is subdominant anyway. It behooves us to turn our attention, then, to other data sets that may be sensitive to these bins in the hope of strengthening our confidence in these constraints. We do this in the next section.

Before we proceed, however, we note that this is not

the first work to find a 2σ exclusion of GR at small scales and low redshift. Reference [9] reports a similar result for their parametrization χ_{II} (see Section IVB of that work). One curious difference, though, is that their analysis shows a preference for $\mathcal{G} < 1$ (their Σ is equivalent to our \mathcal{G}), whereas our Fig. 3(d) shows a clear preference for $\mathcal{G} > 1$. This difference can be traced to the different k binning schemes. The discussion in [9] attributes the preference for non-GR \mathcal{G} as a means to fit a systematic bump in the CFHTLS weak lensing data at large scales (see their Fig. 8; they state that the CFHTLS team ascribes this to residual systematics; also see Sec. 4.3 of [14]). They divide their k bins at $k = 0.1 h \text{ Mpc}^{-1}$. This is approximately where the bump in the CFHTLS data occurs (for $z \lesssim 1$). The MCMC code exploits this by selecting a large value of Ω_m to increase the overall lensing amplitude and fit the bump at large scales (and low k) while reducing the value of \mathcal{G} in the small scale (large k) bin to prevent that increased amplitude from spoiling the fit to the smaller scale data. This allows them to alter the shape of the weak lensing power spectrum to rise and fall with the data. Since we divide the k bins at $k = 0.01 \text{ Mpc}^{-1}$, however, the same shift in parameters would suppress growth, and hence weak lensing power, over too large a range of angles.

Figure 4 illustrates this, as well as recreating Fig. 8 of [9]. While the curve that divides k bins at $k = 0.1 \text{ Mpc}^{-1}$ roughly fits the shape of the systematic feature between 60 and 180 arcminutes, the curve that uses a division at $k = 0.01 \text{ Mpc}^{-1}$ is actually a worse fit than the GR result.

However, the main influence leading to our apparent detection of a departure from GR is actually due to the behavior of the small-angle CFHTLS data (which [9] excludes out of deference to the uncertainties of non-linear modified gravity), as can be seen in Fig. 5. Each of the curves in this figure is generated with identical cosmological parameters ($h = 0.719$, $\Omega_m = 0.25$, and the primordial scalar perturbation amplitude, rather than σ_8 , is also fixed; an exception to this last rule is made for the dashed red curve, as discussed in the caption). Post-GR parameters are all set to zero except the high k – high z value of $\mathcal{V} - 1$ and the high k – low z value of $\mathcal{G} - 1$, which are chosen according to the relationship (which approximately follows the degeneracy direction of the contours drawn in that parameter space) $\mathcal{G} - 1 = -0.2(\mathcal{V} - 1) + 0.06$. One sees that decreasing $\mathcal{V} - 1$ allows the model to better reproduce the precipitous rise of $\langle M_{ap}^2 \rangle$ towards small angles. Such small values of $\mathcal{V} - 1$ also reduce the value of σ_8 predicted. The attempt to fit the steep rise in the CFHTLS data not only drives σ_8 down but this in turn then affects other cosmological parameters.

Figure 6 plots the constraint contours in $\Omega_m - \sigma_8$ space both for post-GR and unmodified GR models. The freedom in the post-GR parameters erases the usual degeneracy between Ω_m and σ_8 seen in GR, replacing it with a degeneracy between σ_8 and our post-GR parameters, while shifting Ω_m . Overall, the MCMC code including

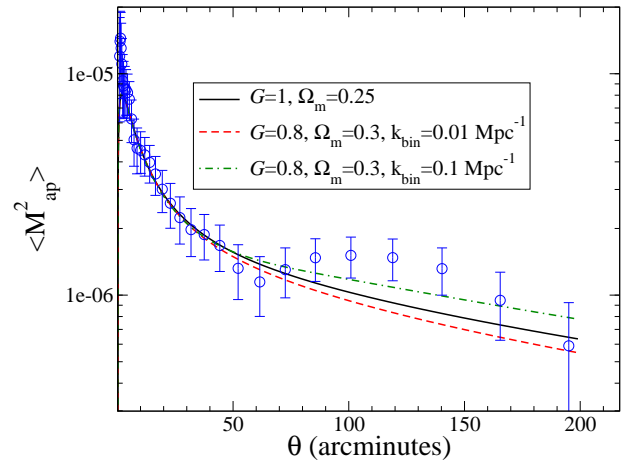


FIG. 4: The square of the aperture mass (see Eq. 5 of [14]) is plotted for different cosmological models in comparison to data from the CFHTLS survey. The solid, black curve shows the results from the Λ CDM concordance model in GR. One can match the small angle behavior by suppressing growth through decreasing the gravitational coupling \mathcal{G} , but increasing growth by increasing Ω_m . Exploring the larger angular scales, the dashed, red curve shows the effect of changing $\mathcal{G}(k > 0.01 \text{ Mpc}^{-1}; z < 1)$ while compensating Ω_m . The dot-dashed, green curve shows the case for $\mathcal{G}(k > 0.1 \text{ Mpc}^{-1}; z < 1)$ as taken in Fig. 8 of [9]. Because this parametrization divides k bins in the midst of the scales probed by the data, this curve fits better the (possibly spurious) bump in $\langle M_{ap}^2 \rangle$ seen in the data between 60 arcmin $< \theta < 180$ arcmin. Data is taken from Table B2 of [14].

CFHTLS data is led to prefer much smaller values of σ_8 than are allowed in GR. This extreme shift due to the small angle CFHTLS data, and the parametrization-dependence exhibited in Fig. 4 due to the CFHTLS data bump, give two strong reasons to doubt the significance of the exclusion of GR in Fig. 3(d). Because CFHTLS represents the largest current weak lensing data set, we continue to use it in the analysis despite these puzzling behaviors. However, we will return to these issues in the next section and see that COSMOS weak lensing data (and CFHTLS data above $10'$ with regard to the σ_8 shift) does not exhibit these deviations.

III. GALAXY AUTO- AND CROSS-CORRELATIONS

In order to get useful constraints on redshift- and scale-dependent deviations from GR, we will need to go beyond the basic data sets used so far: WMAP CMB power spectra [13], Union2 supernovae distances [6], and CFHTLS weak lensing [14]. In particular, different types of cosmological probes, more sensitive to density growth, could be useful.

As discussed in Section II of [19], the CMB anisotropy

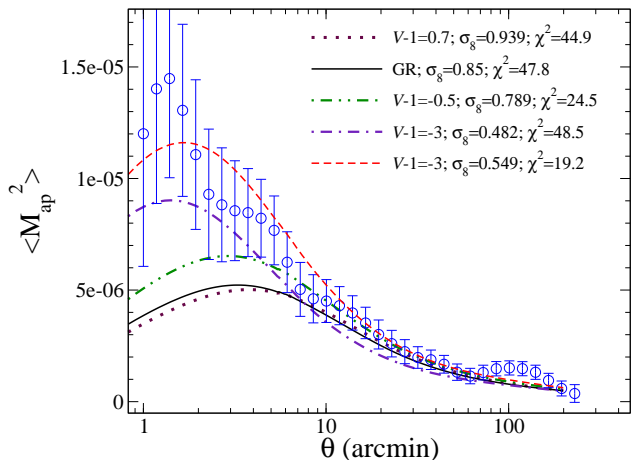


FIG. 5: A view of the data in Fig. 4 with a log scale in θ to zoom in on small angles. The theory curves use bins divided at $k_{\text{bin}} = 0.01 \text{Mpc}^{-1}$, and each is generated with identical background cosmology parameters, fixing the amplitude of the primordial scalar perturbations, so that different post-GR parameter values give different values of σ_8 . Labeled values of $\mathcal{V} - 1$ are set in the high k – high z bin. Values of $\mathcal{G} - 1$ in the high k – low z bin are then given by the approximate degeneracy relation $\mathcal{G} - 1 = -0.2(\mathcal{V} - 1) + 0.06$. All other post-GR parameters are set to zero. To fit the rise at small angles, much steeper than in GR, requires very negative \mathcal{V} and hence low σ_8 . Even raising the primordial perturbation amplitude (dashed red curve) cannot bring σ_8 into the usual range. Values of χ^2 reported in the legend are calculated naively assuming a diagonal covariance matrix using the error bars shown. The four smallest-scale data points are excluded from the χ^2 calculation.

spectrum gives poor constraints on modified gravity. Note the amorphous, two-lobed shape of the CMB plus supernovae contours in Figs. 6-9 of that work. This is because the ISW term in the CMB auto-correlation goes as $(\dot{\phi} + \dot{\psi})^2$ and is thus unaware of sign changes induced by extreme values of \mathcal{G} and \mathcal{V} (or in previous works ϖ). The introduction of weak lensing statistics alleviates some of this uncertainty. However, much of that ground is lost to the introduction of the second post-GR parameter (see Fig. 2).

To proceed further, we need to include measurements that involve more of the interesting physics of modified gravity – further relations between ϕ , ψ , and Δ_m . The two probes we add are the cross-correlation of CMB temperature fluctuations with the galaxy density field and the auto-correlation of the density field, i.e. the galaxy power spectrum.

Section II of [20] discusses the theory of temperature-galaxy cross-correlations. See also Section IV of [21] for a discussion of how this theory is altered in non-GR gravity. The salient point is elucidated in Eqs. (4-6) of [20]: temperature-galaxy cross-correlations constrain cosmological parameters by comparing the matter fluctuations

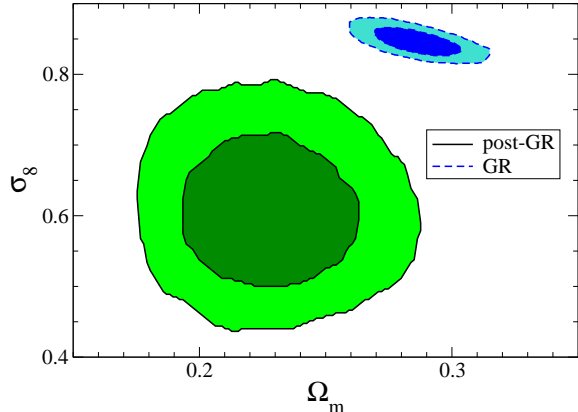


FIG. 6: The 68% and 95% cl contours in Ω_m - σ_8 space for WMAP7, Union2, and CFHTLS data in the case of our post-GR parametrization (solid, green contour) and in the case of GR (dashed, blue contour). The inclusion of post-GR parameters seems to eliminate the degeneracy evident in the GR case and pulls the contours to lower values of σ_8 . This is due to the influence of the steeply rising small-scale CFHTLS data, as illustrated in Fig. 5.

Δ_m traced by the galaxy distribution with the sources for the metric fluctuations ϕ and ψ responsible for the ISW effect. Because this ISW effect (not its auto-correlation in the CMB anisotropy) goes as an integral over redshift of $\dot{\phi} + \dot{\psi}$ times the matter density fluctuation, the cross-correlation measurement ends up depending on only one factor of $\dot{\phi} + \dot{\psi}$. Thus, these measurements ought to be sensitive to the sign changes that get hidden in the CMB anisotropy spectrum.

It is even likely that temperature-galaxy (Tg) cross-correlation data will meaningfully constrain \mathcal{V} , since, at the small scales considered, the

$$\mathcal{V} \equiv \mu(1 + \varpi)$$

term in the $\ddot{\Delta}_m$ growth equation (A5) of [1] becomes dominant, all other modified gravity terms being suppressed as $(\mathcal{H}/k)^2$.

References [20, 22] provide a module to incorporate cross-correlations of the WMAP temperature maps with galaxy survey data from the 2-Micron All Sky Survey, the Sloan Digital Sky Survey, and the NRAO VLA Sky Survey into COSMOMC. We modify this module to accommodate non-GR values of \mathcal{V} and \mathcal{G} and include it into our modified COSMOMC. We excise the module code for incorporating weak lensing of the CMB described in [22], so as to obtain a clearer picture of the impact of Tg information.

Several works have already applied Tg correlations to the question of constraining modified gravity. Reference [23] used Tg data to constrain DGP gravity models. They found, as in [20], that the principal advantage

to this data was in constraining models with nonzero Ω_k . Reference [24] considered $f(R)$ gravity and found significant improvement over previous constraints using just the CMB, though they also found that galaxy cluster abundances gave constraints that were stronger still. These results would seem to indicate that Tg data is not as useful at testing gravity as more direct measurements of the matter power spectrum.

However, these studies were carried out in the contexts of specific gravity theories in which the relationship between high and low k is forced by the theory. Since we make no such assumption, we expect (and find) that inclusion of the Tg data significantly improves constraints on our high k post-GR parameters. Indeed, [21] included Tg data in their exploration of a model-independent parametrization based on \mathcal{V} (which they call Q) and ϖ (their $R \equiv 1 + \varpi$). Their parameters exhibited a similar degeneracy to that discussed in Sec. II A, however the linearity of Tg correlations in $(\phi + \psi)$ still allowed them to place tighter constraints on the difference $\mathcal{V} - \varpi$ than CMB and supernova data alone (see their Table 1 and Figs. 5-6).

We also include measurements of the galaxy-galaxy (gg) auto-correlation power spectrum of luminous red galaxies taken from data release 7 of the Sloan Digital Sky Survey and incorporated into COSMOMC by a publicly available module [25]. These measurements should principally be sensitive to \mathcal{V} since they are more directly measurements of Δ_m than of $\phi + \psi$, and they are taken at scales $k \geq 0.01 \text{ Mpc}^{-1}$.

At small k , adding temperature-galaxy (Tg) and galaxy-galaxy (gg) correlation data produces little change in the constraints on \mathcal{V} and \mathcal{G} vis-à-vis Figs. 3(a) and 3(b). WMAP constraints from the ISW effect dominate at low k , plus there are no galaxy-galaxy data points at $k \lesssim 0.03 h \text{ Mpc}^{-1}$ (see Fig. 8 of [25]).

For large k , however, where the CMB provides generally poor constraints, the addition of temperature-galaxy and galaxy-galaxy data can significantly alter limits on our post-GR parameters. Figure 7 illustrates two examples of this. Figure 7(a) shows the strengthening of constraints in the 95% cl contour from Fig. 3(c) upon incorporating as well the temperature-galaxy data, and the Tg plus galaxy-galaxy data. With current galaxy-galaxy data, most of the improvement is due to Tg, but one can anticipate that as larger galaxy surveys including next generation surveys are completed then galaxy power spectra will become an important ingredient in testing gravity (see Sec. IV for future projections). In particular, \mathcal{V} is still not well determined now.

Conversely, Fig. 7(b) shows the effects of adding Tg, and then Tg plus gg, can for some variables shift the contours instead of tightening them. This may represent a certain tension between data sets; it is interesting to note that Fig. 7(b) finds deviation from GR at the 95% cl, and we return to the role of CFHTLS tension in this below.

Figures 8 update all of the plots in Figs. 3 using all of

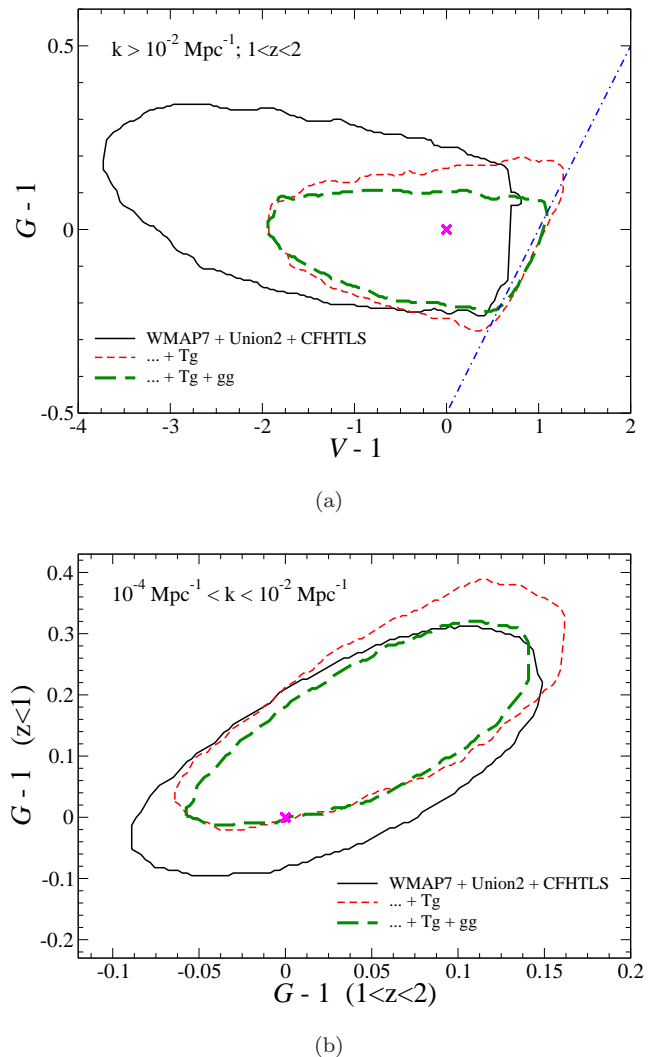


FIG. 7: [Top panel] 95% cl contours in \mathcal{V} - \mathcal{G} space for the high k , high z bin are compared for three different combinations of data sets. The solid, black contour shows the results from Fig. 3(c) using CMB, supernovae, and weak lensing data. The thin-dashed, red contour adds temperature-galaxy (Tg) cross-correlation data from [20]. The thick-dashed, green contour further adds galaxy-galaxy (gg) correlation data from [25]. The diagonal, dot-dashed line gives the $\mu = 0$ boundary. As datasets are added, the contours close in on GR parameter values (the magenta x). Current galaxy correlation data is not yet sensitive enough though to put a meaningful constraint on \mathcal{V} . [Bottom panel] Addition of data sets can sometimes shift rather than tighten the contours, as shown here in $\mathcal{G}(1 < z < 2)$ - $\mathcal{G}(z < 1)$ space for the low k bin. Note that with the additional data GR now lies on the edge of the 95% cl region.

the data sets discussed. The results are the foreground, blue contours. We see that \mathcal{G} is constrained with an uncertainty of roughly 0.1, while \mathcal{V} is unknown to within ~ 1 . All cases, except high k - high z , have pulled further off the $\mu = 0$ restricted area. Note that the 95% cl contour in the high k - low z bin, Fig. 8(d) using CFHTLS

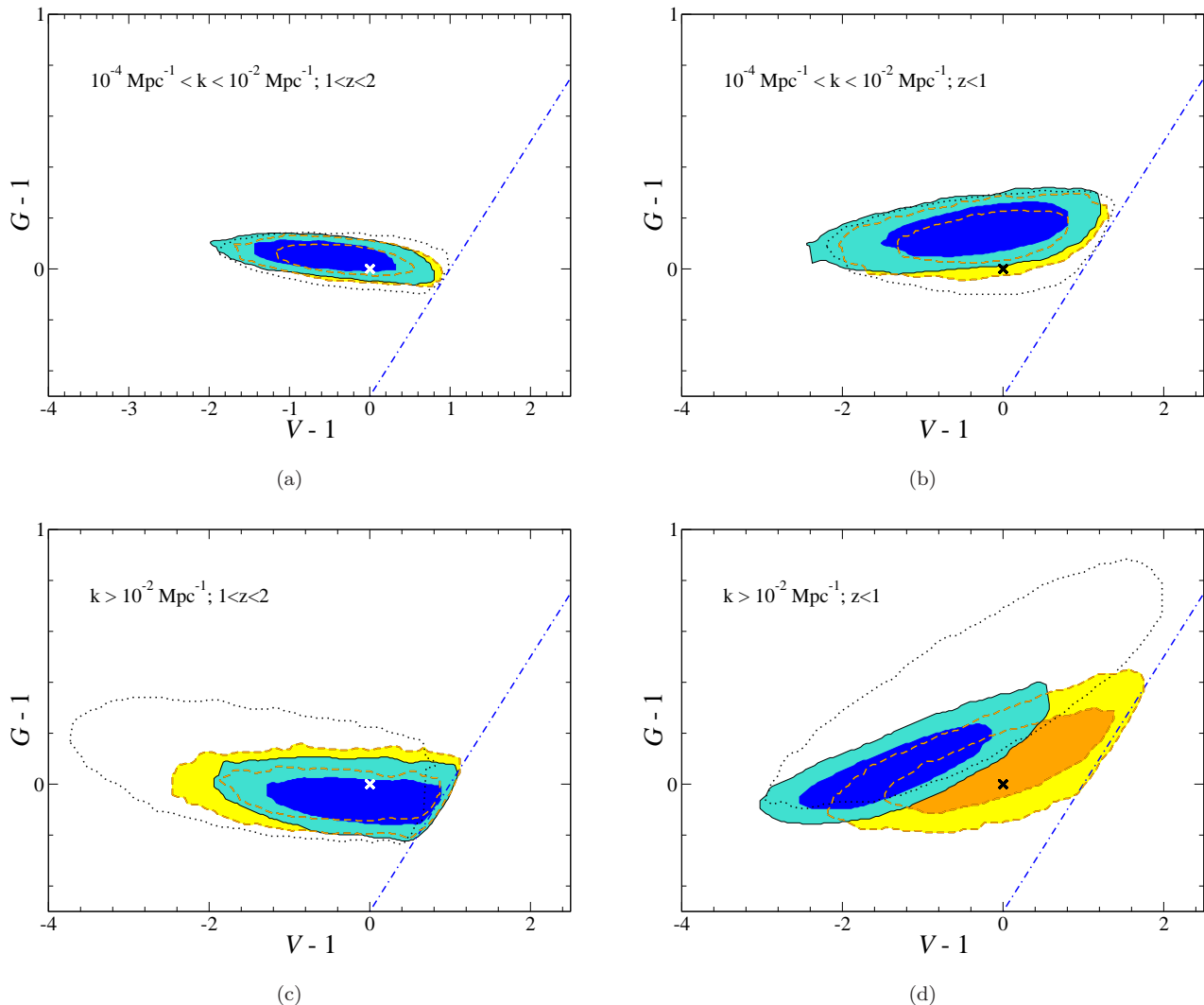


FIG. 8: 68% and 95% cl constraints on $\mathcal{V}-1$ and $\mathcal{G}-1$ are plotted for the two redshift and two wavenumber bins, using CMB, supernovae, weak lensing, T_g , and g_g data. Foreground, blue contours use CFHTLS weak lensing data. Background, yellow contours use COSMOS weak lensing data. The dotted contours reproduce the 95% cl contours without T_g or g_g data from Figs. 3. The diagonal, dot-dashed line gives the $\mu = 0$ boundary, from which the low k contours at least have now pulled away. The x 's denote GR values. Both k bins at low z exhibit some preference for non-GR parameter values when using CFHTLS, but not when using COSMOS, weak lensing data.

data, still excludes General Relativity, although as we have stated this is possibly due to systematics in the CFHTLS weak lensing data. It now appears that the low k – low z bin also prefers non-GR values of our parameters, though in this case the apparent exclusion of GR is just at 95% cl. Since this effect did not manifest itself until we added the galaxy-based datasets, this could either be an effect of systematic tension between galaxy-count measurements and other data sets, or a true restriction from the increased precision. Note that Fig. 7(b) gives another view of the low k – low z deviation in \mathcal{G} .

To test the hypothesis that the exclusion of GR at low z is due to systematic effects in the CFHTLS data, we plot the same constraints substituting weak lensing data

from the COSMOS survey [7] in the place of CFHTLS data. COSMOS constraints are the background, yellow contours in Fig. 8. The constraints in the low k bins appear almost unaffected by this substitution (though the low k – low z bin no longer hints at an exclusion of GR, as it did in the case of the CFHTLS data). This should not be surprising. The low k bins correspond to scales where the WMAP7 data has a lot of constraining power. The high k – high z bin also appears moderately insensitive to which weak lensing set is used. In the high k – low z bin, though, we find that the 99% cl exclusion of GR vanishes when COSMOS is used, and GR instead lies comfortably within the 68% cl contour. This could mean that the COSMOS data is less subject to spuri-

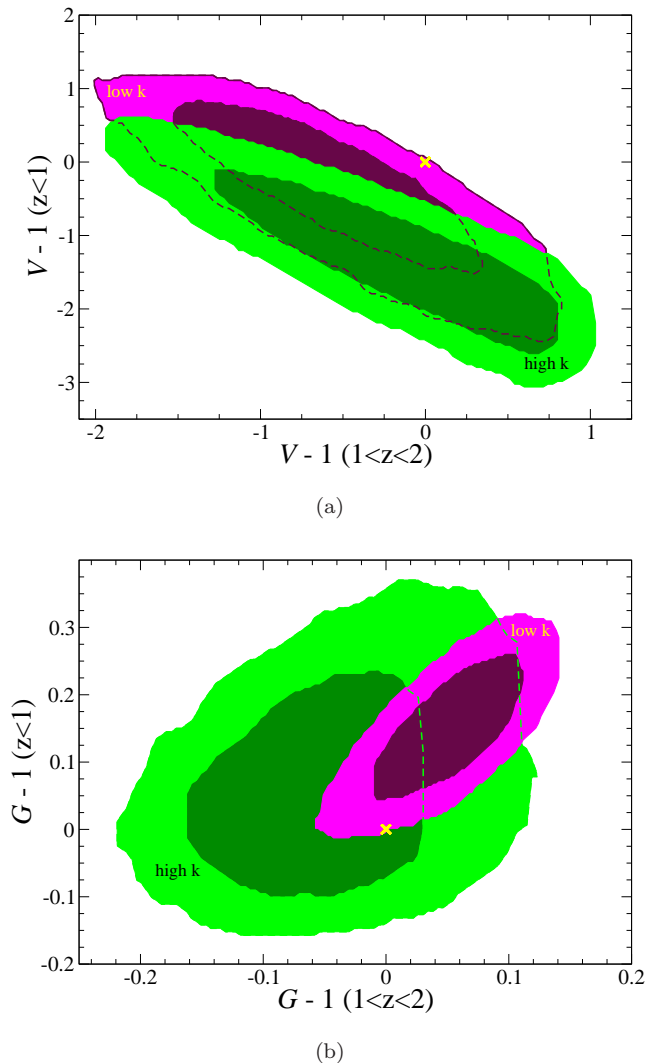


FIG. 9: 68% and 95% cl constraints on the correlations of $\mathcal{V}-1$ (top panel) and $\mathcal{G}-1$ (bottom panel) between redshift bins, using CMB, supernovae, weak lensing (CFHTLS), Tg, and gg data. Contours are labeled according to k binning. The x's denote GR values. The high k case of \mathcal{V} exhibits a deviation from GR, corresponding to a different growth amplitude.

ous systematic effects. Note that the combination using COSMOS data is somewhat less constraining due to the small sky area of COSMOS. It will be interesting to see what results occur once we have data from larger, more detailed future weak lensing surveys.

We can also reexamine the redshift dependence of each of the post-GR parameters. Figures 9 plot the correlations between redshift bins for \mathcal{V} and \mathcal{G} , for each bin of wavenumber k using CFHTLS data. The values of \mathcal{G} for low k are positively correlated, as found before for scale-independent \mathcal{G} , while for high k the values are rather independent. This can be understood by considering that the small k bin has the greatest effect on the ISW imprint in the CMB. Since the ISW effect goes as $(\dot{\phi} + \dot{\psi})^2$,

the CMB data will prefer parameter combinations that minimize the change in \mathcal{G} across redshift bins. Because the large k bin encompasses scales over which the ISW effect is subdominant, such a preference is not operative there.

For \mathcal{V} there is negative correlation as before, for both low and high k . This is a manifestation of the role of \mathcal{V} in regulating the growth of structure, i.e. Δ_m . The low k contours in Fig. 9(a) have a main degeneracy direction parallel to lines with a slope in $\{\mathcal{V}(1 < z < 2), \mathcal{V}(z < 1)\}$ space of ~ -1.3 . The high k contours have a degeneracy direction of approximate slope ~ -1.2 . Integrating Eq. (A5) of [1] for values of Ω_m close to those favored by WMAP and Union2 ($\Omega_m \sim 0.25$), one finds that (independent of \mathcal{G} and H_0) values of $\{\mathcal{V}(1 < z < 2), \mathcal{V}(z < 1)\}$ that lie along lines with slopes ranging between -1.3 and -1.4 return values of the relative growth $\Delta_m(z=0)/\Delta_m(z=100)$ that are similar to within a few percent. Displacement perpendicular to this direction controls the absolute growth factor. The offset of the high k contours from the low k contours (and from GR), signifies a preference for suppressed growth relative to GR in the high k modes; GR lies outside the 95% cl contour in the high k bin. Again, this could be due to the odd bump in the CFHTLS weak lensing power or the steep rise towards small angles in Fig. 5. Figures 10 show the effect of using COSMOS weak lensing data instead of CFHTLS data on the correlations of $\mathcal{V}-1$ and $\mathcal{G}-1$ across redshift bins. As before, the exclusion of GR vanishes.

As in the scale-independent case, we find that our post-GR parameters correlate most strongly with σ_8 out of all of the usual cosmological parameters. Once again, larger \mathcal{V} amplifies growth and induces a larger σ_8 while larger \mathcal{G} brings lower values of σ_8 into agreement with the data. These correlations are only manifest in the high k bin, indicating that they are principally dependent on the weak lensing, Tg, and gg data sets. The correlation with \mathcal{V} appears in the high z bin, as expected due to the cumulative effect of growth over time (see discussion in Sec. II C). In the case of \mathcal{G} , probing the potentials, the correlation with σ_8 appears in the low z bin, as expected for the weak lensing data weighted toward $z < 1$. The shift to low σ_8 as seen in Fig. 6 does not occur when COSMOS data is used, or when CFHTLS data is restricted to $\theta > 10'$.

IV. CONSTRAINTS POSSIBLE WITH FUTURE DATA

Given the weak constraints on \mathcal{V} in Fig. 8, and possible hints of deviations from GR, it is important to investigate the capabilities of future galaxy surveys. These should provide us with more direct measurements of, and much better precision on, the growth of density perturbations through the galaxy power spectrum, testing GR and improving our knowledge of post-GR parameters.

We consider the specific example of BigBOSS [26], a proposed ground-based survey intended to constrain

cosmology by measuring the baryon acoustic oscillations and redshift space distortions in the galaxy distribution. Reference [27] explored BigBOSS tests of gravity (and dark sector physics) in terms of the gravitational growth index γ [10], using a Fisher matrix calculation. Here, we carry out a more sophisticated Markov Chain Monte Carlo fit to simulated data, allowing for scale- and time-dependence in the gravitational modifications through our binned k , binned z post-GR parameters.

We generate our mock BigBOSS data around the Λ CDM, GR ($\mathcal{V} = \mathcal{G} = 1$) maximum likelihood cosmology of WMAP7. The data is considered in the form of measurements of the redshift-distorted galaxy-galaxy power spectrum

$$P_g(\vec{k}; z) = P_g(k, \mu; z) = (b + f\mu^2)^2 P(k; z), \quad (11)$$

where P is the power spectrum of matter overdensities, b is the linear bias relating the overdensity of galaxy counts to the overdensity of matter, $f = d \ln \Delta_m(k, a) / d \ln a$ is the growth factor, and μ is the cosine of the angle \vec{k} makes with the line of sight.

We take survey parameters, including galaxy number densities, from [28], and consider emission line galaxies (ELG) and luminous red galaxies (LRG) as two separate data sets. The bias b is a function of redshift,

$$b(z) = b_0 \frac{\Delta_m(k, z=0)}{\Delta_m(k, z)}, \quad (12)$$

where b_0 is a nuisance parameter to be marginalized over for each data set. The fiducial values are $b_{0,\text{ELG}} = 0.8$ and $b_{0,\text{LRG}} = 1.7$. The values and redshift dependence are good fits to current galaxy observations, and can be motivated by comoving clustering models [29].

In calculating the galaxy power spectrum we consider modes $10^{-4} < k < 10^{-1} \text{Mpc}^{-1}$. As in [30], we assume that the covariance matrix of P_g is diagonal with

$$C_{ij} \approx 16\pi^3 \delta_{ij} \delta_{mn} \frac{P_g(k_i, \mu_m) P_g(k_j, \mu_n)}{V_0 d^3 k} \times \left[\frac{1 + \bar{n} P_g(k_i, \mu_m)}{\bar{n} P_g(k_i, \mu_m)} \right]^2 \quad (13)$$

where V_0 is the real space volume of the survey and \bar{n} is the selection function of the survey as a function of comoving distance r . Thus, the likelihood \mathcal{L} for a cosmological model which predicts galaxy-galaxy power spectrum $\hat{P}_g(k, \mu)$ is given by

$$-2 \ln[\mathcal{L}] = \frac{1}{4\pi} \int dz \frac{dr}{dz} r^2 \int d \ln k k^3 \times \int d\mu \frac{(\hat{P}_g - P_g)^2}{P_g^2} \left(\frac{\bar{n}(r) P_g}{1 + \bar{n}(r) P_g} \right)^2 \quad (14)$$

We also include mock Planck CMB data generated with the COSMOMC module FuturCMB [31, 32] and mock future supernova data based on a space survey of

1800 supernovae out to $z = 1.5$ (“JDEM”) in our projected data MCMC calculation. For computational efficiency we do not consider the gravitational lensing of the CMB.

Figures 11 show the 68% and 95% confidence limit contours resulting from the full MCMC calculation on our mock data sets. There is an order of magnitude or more improvement in the constraint placed on \mathcal{V} in all bins by including BigBOSS. As in [27], we find that BigBOSS will be able to constrain departures from the growth history of GR (here parametrized as $\mathcal{V} - 1$, there by γ) to within $\sim 10\%$. Constraints on \mathcal{G} also improve, though by more modest factors.

V. CONCLUSIONS

The suite of current cosmological data has grown to the point that increasingly sophisticated model-independent extensions to general relativity can be tested. This includes both time- and scale-dependent modifications; we utilize bins in redshift z and wavemode k for localization of the effects and clarity of physical interpretation. The functions \mathcal{G} and \mathcal{V} investigated here in detail, giving a complete model-independent description (together with stress-energy conservation) of the gravitational modifications, are closely tied to the sum of the metric potentials and to the matter growth, respectively. They also have the virtue of being substantially decorrelated from each other. On the other hand, correlations across redshift or across length scales can be easily studied, giving deeper insight into the effects of the modifications and where they show up in the observations.

Using current CMB, supernova, and weak lensing data from CFHTLS we find an inconsistency with general relativity at near the 99% confidence limit at $k > 0.01 \text{Mpc}^{-1}$ and $z < 1$. Through a series of investigations we identify its origin as being due to an abnormally steep rise in the weak lensing power at small scales. This rise strongly shifts \mathcal{V} from the GR value and also drives down the estimated value of σ_8 . The CFHTLS data also shows an unusual bump in the power at larger scales. By replacing the CFHTLS measurements with COSMOS weak lensing data, we find that all these deviations vanish and that GR provides an excellent fit. Thus, the deviations may originate in systematic effects in the CFHTLS data (a possibility also raised by members of the CFHTLS team) interacting with increased freedom from the post-GR parameter fitting.

The addition of galaxy clustering measurements, through both the CMB temperature-galaxy count (Tg) and galaxy-galaxy power spectrum (gg) statistics, tightens the constraints on smaller scales (high k). This improvement is especially noticeable in \mathcal{V} , since it enters in the matter growth. Again, the full combination using CFHTLS data shows significant deviations, which go away on substitution with COSMOS data.

Given the important role of galaxy survey data, and

the still weak constraints on the \mathcal{V} deviation parameter (only of order unity), we examine the potential leverage of future galaxy survey measurements, specifically from BigBOSS. These appear quite promising for confronting general relativity with further measurements, giving a direct probe of growth and one that could be highly precise from the large statistics. Together with Planck CMB and supernovae data, such a galaxy survey could improve the area uncertainty on the post-GR parameters in each of four bins of redshift-scale by factors from 10 to 100. This is an exciting prospect as we seek to understand gravity as the most pervasive and dominant force in the universe.

Acknowledgments

We thank Tristan Smith for helpful discussions and insight and Chanju Kim for timely hardware fixes. We ac-

knowledge use of NASA's Legacy Archive for Microwave Background Data Analysis (LAMBDA). This work has been supported by the World Class University grant R32-2009-000-10130-0 through the National Research Foundation, Ministry of Education, Science and Technology of Korea. EL has been supported in part by the Director, Office of Science, Office of High Energy Physics, of the U.S. Department of Energy under Contract No. DE-AC02-05CH11231.

-
- [1] S.F. Daniel, E.V. Linder, T.L. Smith, R.R. Caldwell, A. Cooray, A. Leauthaud, L. Lombriser, *Phys. Rev. D* **81**, 123508 (2010) [arXiv:1002.1962].
- [2] C. P. Ma and E. Bertschinger, *Astrophys. J.* **455**, 7 (1995) [arXiv:astro-ph/9506072].
- [3] J. Dunkley *et al.* [WMAP Collaboration], *Astrophys. J. Suppl.* **180**, 306 (2009) arXiv:0803.0586 [astro-ph].
- [4] M. R.olta *et al.* [WMAP Collaboration], *Astrophys. J. Suppl.* **180**, 296 (2009) [arXiv:0803.0593 [astro-ph]].
- [5] G. Hinshaw *et al.* [WMAP Collaboration], *Astrophys. J. Suppl.* **180**, 225 (2009) [arXiv:0803.0732 [astro-ph]].
- [6] R. Amanullah *et al.*, *Astrophys. J.* **716**, 712 (2010) [arXiv:1004.1711].
- [7] R. Massey *et al.*, *Astrophys. J. Suppl.* **172**, 239 (2007) [arXiv:astro-ph/0701480].
- [8] Y-S. Song, L. Hollenstein, G. Caldera-Cabral, K. Koyama, *JCAP* 1004, 018 (2010) [arXiv:1001.0969].
- [9] G. B. Zhao *et al.*, *Phys. Rev. D* **81**, 103510 (2010) [arXiv:1003.0001 [astro-ph.CO]].
- [10] E.V. Linder, *Phys. Rev. D* **72**, 043529 (2005) [arXiv:astro-ph/0507263].
- [11] E. V. Linder and R. N. Cahn, *Astropart. Phys.* **28**, 481 (2007) [arXiv:astro-ph/0701317].
- [12] G.B. Zhao, L. Pogosian, A. Silvestri, J. Zylberberg, *Phys. Rev. Lett.* **103**, 241301 (2009) [arXiv:0905.1326].
- [13] N. Jarosik *et al.*, arXiv:1001.4744 [astro-ph.CO].
- [14] L. Fu *et al.*, *Astron. Astrophys.* **479**, 9 (2008) [arXiv:0712.0884 [astro-ph]].
- [15] A. Lewis, A. Challinor and A. Lasenby *Astrophys. J.* **538**, 473 (2000) [arXiv:astro-ph/9911177].
- [16] A. Lewis and S. Bridle, *Phys. Rev. D* **66**, 103511 (2002) [arXiv:astro-ph/0205436].
- [17] A. Lewis and S. Bridle, <http://cosmologist.info/notes/COSMOMC.ps.gz>
- [18] J. Lesgourgues, M. Viel, M. G. Haehnelt and R. Massey, *JCAP* **0711**, 008 (2007) [arXiv:0705.0533 [astro-ph]].
- [19] S. F. Daniel, R. R. Caldwell, A. Cooray, P. Serra, A. Melchiorri, *Phys. Rev. D* **80**, 023532 (2009) [arXiv:0901.0919 [astro-ph.CO]].
- [20] S. Ho, C. Hirata, N. Padmanabhan, U. Seljak and N. Bahcall, *Phys. Rev. D* **78**, 043519 (2008) [arXiv:0801.0642 [astro-ph]].
- [21] R. Bean and M. Tangmatitham, *Phys. Rev. D* **81**, 083534 (2010) [arXiv:1002.4197 [astro-ph.CO]].
- [22] C. M. Hirata, S. Ho, N. Padmanabhan, U. Seljak and N. A. Bahcall, *Phys. Rev. D* **78**, 043520 (2008) [arXiv:0801.0644 [astro-ph]].
- [23] L. Lombriser, W. Hu, W. Fang and U. Seljak, *Phys. Rev. D* **80**, 063536 (2009) [arXiv:0905.1112 [astro-ph.CO]].
- [24] L. Lombriser, A. Slosar, U. Seljak and W. Hu, arXiv:1003.3009 [astro-ph.CO].
- [25] B. A. Reid *et al.*, *Mon. Not. Roy. Astron. Soc.* **404**, 60 (2010) [arXiv:0907.1659 [astro-ph.CO]].
- [26] D. J. Schlegel *et al.*, arXiv:0904.0468 [astro-ph.CO].
- [27] A. Stril, R. N. Cahn and E. V. Linder, *Mon. Not. Roy. Astron. Soc.* **404**, 239 (2010) [arXiv:0910.1833 [astro-ph.CO]].
- [28] D. Schlegel, <http://lamwvs.oamp.fr/cosmowiki/CosmoZsurveyTalks?action=AttachFile&do=get&target=schlegel.pdf>
- [29] J. Newman and N. Padmanabhan, private communications
- [30] M. Tegmark, *Phys. Rev. Lett.* **79**, 3806 (1997) [arXiv:astro-ph/9706198].
- [31] L. Perotto, J. Lesgourgues, S. Hannestad, H. Tu and Y. Y. Y. Wong, *JCAP* **0610**, 013 (2006) [arXiv:astro-ph/0606227].
- [32] <http://lpsc.in2p3.fr/perotto/>

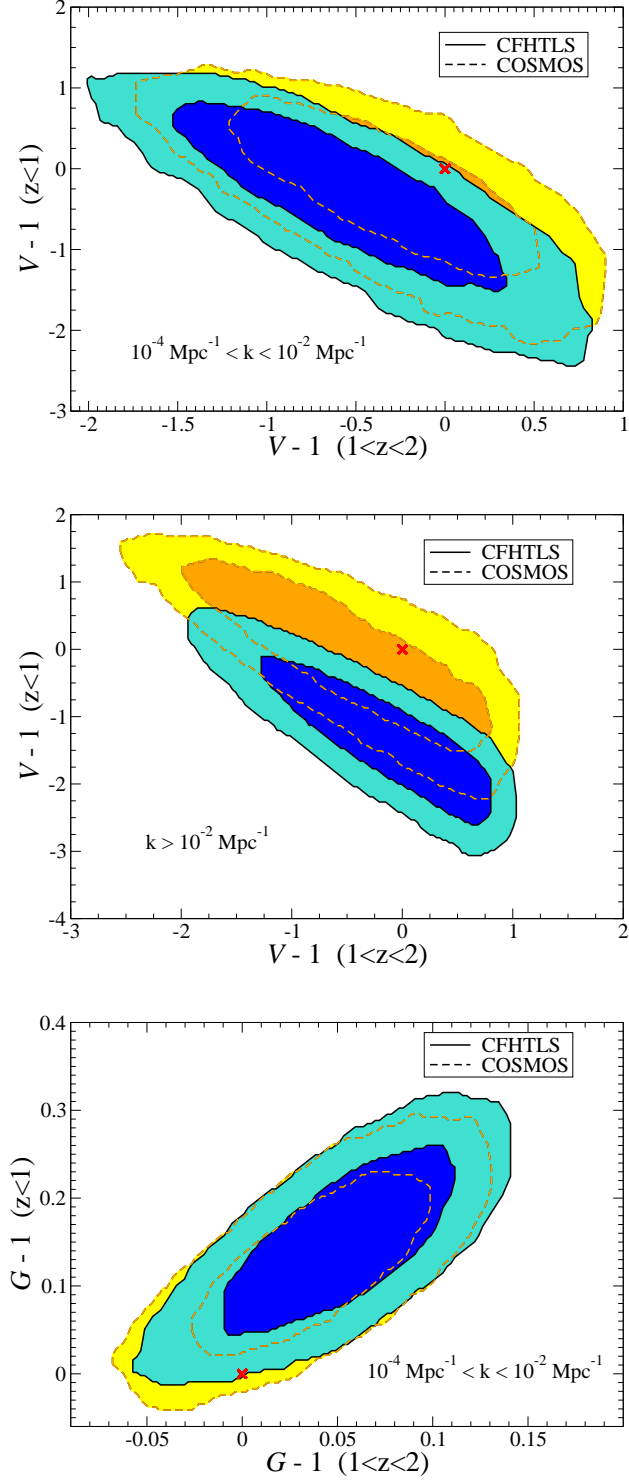


FIG. 10: 68% and 95% cl constraints on the correlations of $\mathcal{V} - 1$ and $\mathcal{G} - 1$ between redshift bins, using CMB, supernovae, weak lensing, T_g , and g_g data. Substituting COSMOS (background) for CFHTLS (foreground) eliminates the apparent exclusion of GR. The x's denote GR values. We do not plot the high k bin correlations for $\mathcal{G} - 1$ as there are no interesting correlations or deviations there.

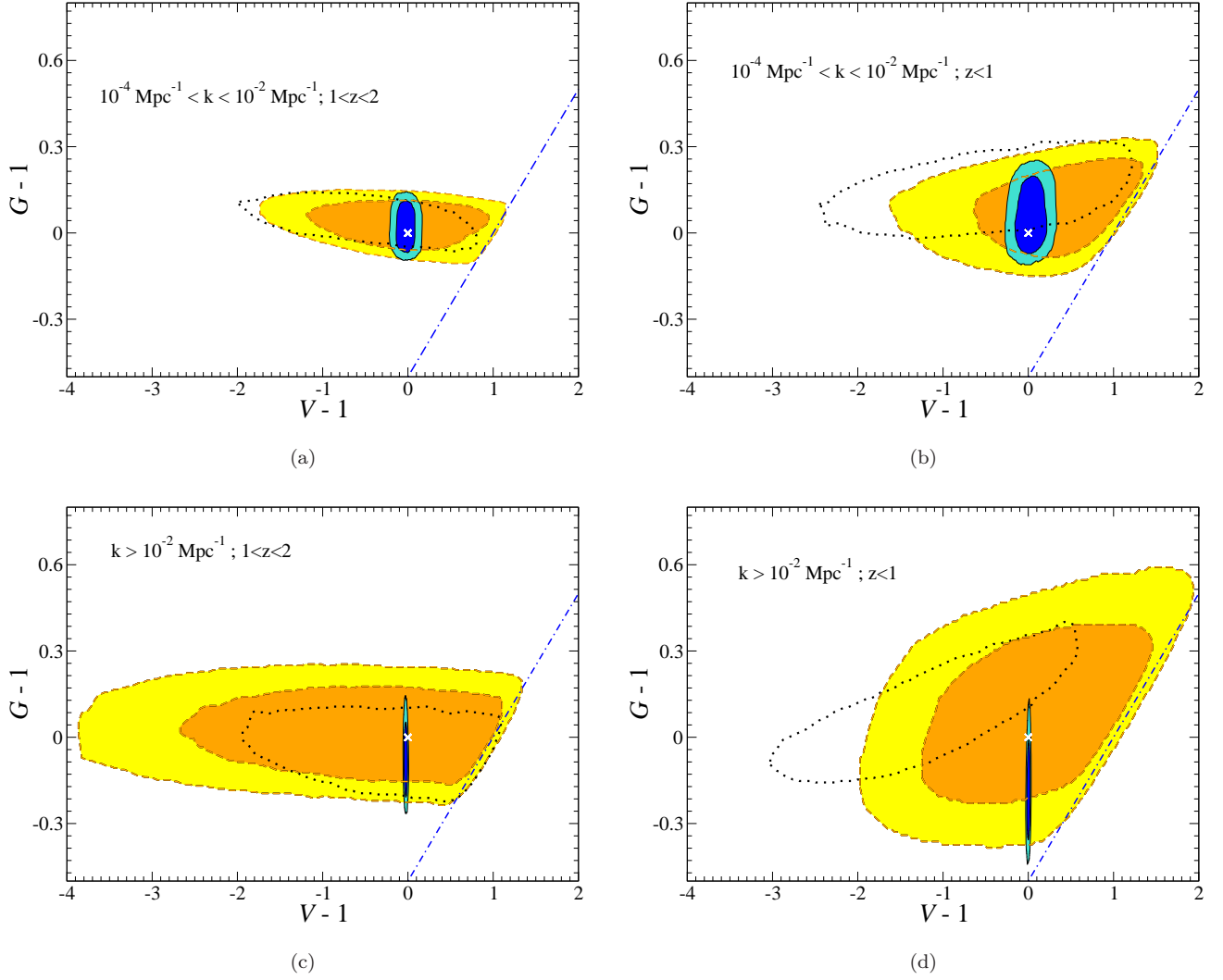


FIG. 11: 68% and 95% cl constraints on $\mathcal{V} - 1$ and $\mathcal{G} - 1$ are plotted for the two redshift and two wavenumber bins using mock future data. Foreground (blue) contours use mock BigBOSS, Planck, and JDEM supernova data. Background (yellow) contours use only mock Planck and JDEM supernova data. The dotted contours recreate the 95% cl current data contours from Figs. 8 (using CFHTLS) to illustrate the expected improvement in constraints. The x's denote the fiducial GR values.